The Single Residue K12 Governs the Exceptional Voltage Sensitivity of Mitochondrial Voltage-Dependent Anion Channel Gating

Van A. Ngo, María Queralt-Martín, Farha Khan, Lucie Bergdoll, Jeff Abramson, Sergey m. Bezrukov, Tatiana K Rostovtseva, David P Hoogerheide, Sergei Yu Noskov

The single residue K12 governs the exceptional voltage sensitivity of mitochondrial voltage-dependent anion channel gating

Van A. Ngo,[†,1,2] María Queralt-Martín[†,3,4] Farha Khan, [†,5] Lucie Bergdoll,[6] Jeff Abramson,[5] Sergey M. Bezrukov,[3] Tatiana K. Rostovtseva,[3] David P. Hoogerheide*[,7], Sergei Yu. Noskov[‡,1]

[1] Center for Molecular Simulations, Department of Biological Sciences, University of Calgary, Calgary, AB, Canada T2N 1N4

[2] Advanced Computing for Life Sciences and Engineering, Computing and Computational Sciences, National Center for Computational Sciences, Oak Ridge National Lab, Oak Ridge, TN 37830

[3] Section on Molecular Transport, *Eunice Kennedy Shriver* National Institute of Child Health and Human Development, National Institutes of Health, Bethesda, MD 20892

[4] Laboratory of Molecular Biophysics, Department of Physics, Universitat Jaume I, 12071 Castellón, Spain.

[5] Department of Physiology, University of California, Los Angeles, CA 90095

[6] LISM UMR 7255, CNRS and Aix-Marseille University, 31 Chemin Joseph Aiguier, Marseille cedex 20 13402, France

[7] Center for Neutron Research, National Institute of Standards and Technology, Gaithersburg, MD 20899

*corresponding author

Email: david.hoogerheide@nist.gov

‡ Deceased

KEYWORDS: MD simulations; x-ray crystallography; single-channel electrophysiology; voltage gating; Brownian Dynamics

ABSTRACT: The voltage-dependent anion channel (VDAC) is a β-barrel channel of the mitochondrial outer membrane (MOM) that passively transports ions, metabolites, polypeptides, and single-stranded DNA. VDAC responds to a transmembrane potential by "gating," *i.e.* transitioning to one of a variety of low-conducting states of unknown structure. The gated state results in nearly complete suppression of multivalent mitochondrial metabolite (such as ATP and ADP) transport, while enhancing calcium transport. Voltage gating is a universal property of β-barrel channels; however, compared to other β-barrel channels, such as bacterial porins and toxins, VDAC gating is extremely sensitive to transmembrane potential. Here, we show that a single residue in the pore interior, K12, is responsible for most of VDAC's voltage sensitivity. Using the analysis of over 40 μs of atomistic molecular dynamics (MD) simulations, we explore correlations between motions of charged residues inside the VDAC pore and geometric deformations of the β-barrel. K12 is bistable; its motions between two widely separated positions along the pore axis enhance the fluctuations of the β-barrel and augment the likelihood of gating. These results are confirmed by single channel electrophysiology of various K12 mutants, which show dramatic reduction of the voltage-induced gating transitions. To reveal any structural basis of the altered gating, we resolved the crystal structure of the K12E mutant at a resolution of 2.6 Å. The architecture of the K12E mutant is similar to the wild type; however, MD simulations using the K12E mutant structure show restricted motion of the mutated residue 12, due to enhanced connectivity with neighboring residues, and diminished amplitude of barrel motions. We conclude that β-barrel fluctuations, governed particularly by residue K12, drive VDAC gating transitions.

Introduction

The voltage-dependent anion channel (VDAC) is the most abundant protein in the mitochondrial outer membrane (MOM) [1-2] and is the primary conduit for ions and water-soluble metabolites such as ATP and ADP to cross the MOM. As such, VDAC plays a central role in regulation of MOM permeability and mitochondrial metabolism, and in communication between mitochondria and the rest of the cell. VDAC is a large-conductance (4 nS at 21 °C in 1 M KCl), weakly anion-selective transmembrane pore allowing the passive transport of charged and neutral species up to ~ 2-5 kDa [3-

[4]. The VDAC channel comprises a 19-stranded β-barrel with a segmented N-terminal α-helix, which is located halfway through the pore of the barrel and is parallel to the membrane surface [5-7]. The two parts of the α-helical domain are referred to as α1 (residues 6 to 10) and α2 (residues 12 to 20). The involvement of specific N-terminal residues in VDAC's gating and selectivity has been previously observed [8-10], but the mechanism of the effect of the α-helical N-terminal domains on VDAC's function remains controversial.

The characteristic and conserved property of VDAC channels reconstituted into lipid membranes and subjected to a transmembrane potential is their ability to "gate", or to transition between a unique high-conductance ("open") state and several low-conductance ("closed") states. The relative conductance change in solutions of monovalent ions upon transitioning to the closed state is typically about a factor of 2, with a reduction in the selectivity of VDAC for anions in its closed state. The effect on multivalent ions and metabolites is more pronounced; VDAC's closed states are virtually impermeable to negatively charged metabolites such as ATP and ADP due to steric and electrostatic barriers [11-13], but are more permeable to calcium ions [14]. Thus, voltage-induced closures of VDAC have been proposed to play an important role in regulation of metabolite and calcium fluxes across the MOM.

Voltage gating is a common property of β-barrel channels, and has been observed in bacterial outer membrane porins [15] as well as in the anthrax [16], aerolysin [17], and α-hemolysin [18] toxins. In contrast to these channels, where gating is observed at transmembrane potentials of 70 mV or higher, the sensitivity of VDAC gating to voltage is extraordinarily sensitive, occurring at 30 mV or lower. In the absence of a general mechanistic understanding of β-barrel gating, the molecular origin of VDAC gating, and particularly its exquisite voltage sensitivity, remains elusive. Structural data on VDAC have not revealed significant variations that are readily identified as open or closed conformations [5-7, 19-21]. The general consensus is that the 3D structures represent the open conformation [22], while a closed state has not yet been structurally characterized, and how VDAC transitions between closed and open states remains unknown.

The search for a mechanism of voltage-induced VDAC gating has focused on identifying a voltage-sensing domain (VSD), analogous to the lipid-encased mobile voltage sensors of ion-selective channels [23]. Movement of the VSD has been proposed to either block the VDAC channel [8, 24-26], thus reducing its conductance, or trigger a reduction in the cross-section of the channel [24, 27-30]. The α-helical domain, being the only domain of VDAC that is not part of the barrel, is a clear candidate for the VSD; however, when α1 is cross-linked to residues in the channel wall, voltage-induced closures are still observed, demonstrating that the N-terminal region is either not a mobile voltage sensor [31] or moves in tandem with the linked residues. Indeed, the existence and molecular identity of a putative voltage sensor in VDAC gating has not been identified by either simulation or experiment [26, 32-34]. Conversely, all 61 charged residues that often affect voltage gating [9-10] are spread throughout the entire structure of VDAC [22] (Figure S1).

In this work, we demonstrate that the voltage sensitivity of VDAC1 (hereafter "VDAC") gating arises from the high-amplitude bistability of a single residue, K12. Atomistic molecular dynamics simulations of VDAC in its open state identify a correlation between the deformation of the VDAC barrel and collective motions of charged residues, especially the bistable residue K12, along the pore axis. Simulations further show that, if residue 12 is mutated to glutamic acid, the bistability disappears, and its range of motion, as well as the correlated barrel fluctuations in the open state, are significantly reduced or restricted. Electrophysiological experiments on VDAC reconstituted into planar lipid membranes confirm that mutation of K12 to neutral or anionic residues dramatically reduces VDAC's voltage response and nullifies or reverses the channel's selectivity. X-ray crystallography reveals no major structural changes or movement of the helix in the pore in the K12E mutant. We conclude that the presence of a lysine at position 12 creates high-amplitude bistable motion of this residue along the pore axis, and due to the mechanical coupling between the channel pore and charged residues, allows for large fluctuations in barrel geometry. It naturally follows that barrel fluctuations are critical for exploring the intermediate structures that lead to VDAC gated states, such that mutation of K12 reduces the barrel fluctuations and hence the rate of VDAC closure. In sum, K12 destabilizes the barrel and sensitizes VDAC for voltage-induced gating transitions.

Results

Molecular dynamics identify K12 as a key residue for VDAC dynamics

Voltage-induced closures of VDAC are relatively rare events. The rate of onset is on the order of seconds to minutes at absolute transmembrane potentials of 50 mV in common lipids [10, 35-36]. The duration of each closure is likewise on the order of seconds. The voltage-dependent kinetics of the closure process are complex and deviate significantly from the hallmarks of a two-state system, suggesting that, in its open state, the channel explores multiple substates without observable changes in the channel conductance [37]. Thus, while atomistic MD simulations are unlikely to directly yield a closed state structure at experimentally relevant potentials, they can interrogate the fast equilibrium dynamics of the VDAC channel in its open substates and identify the key residue(s) whose role in voltage-induced closure can be explored experimentally.

We performed multiple μs-long MD simulations of wild-type (WT) murine VDAC1 (PDB ID: 3EMN) [7] embedded in a voltage-biased dioleoyl-phosphatidylcholine (DOPC) membrane (Figure 1). The transmembrane potential was chosen to be 160 mV

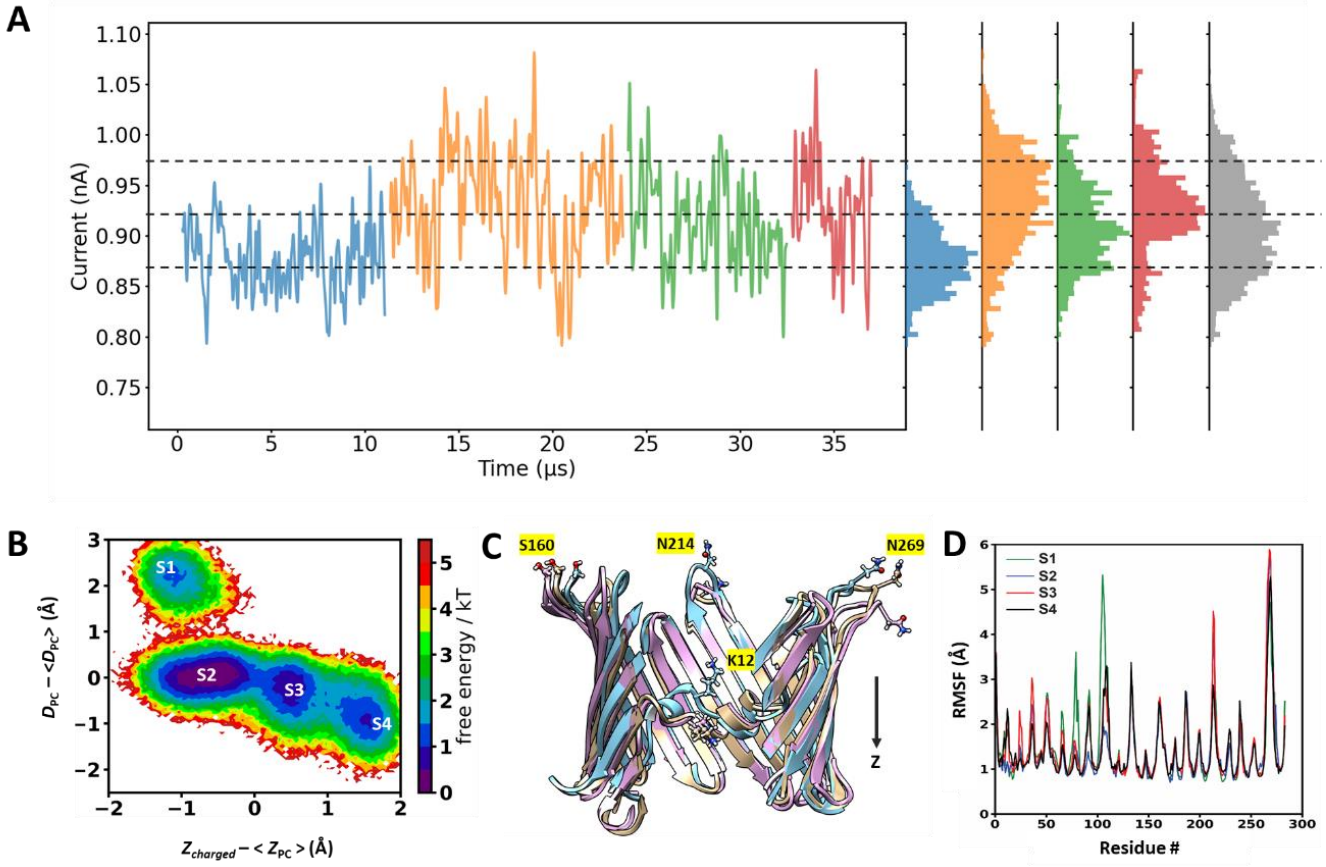

Figure 1. Summary of all-atom MD simulations of WT VDAC1. (A) Time records of ionic current for a VDAC1 channel embedded in a DOPC membrane and subjected to +160 mV transmembrane potential for 4 independent simulations. Instantaneous current is filtered with an 8-pole digital Bessel filter (cutoff frequency 6.9 MHz). Histograms are compatible with the existence of conductance substates (horizontal dashed lines); colors correspond to individual traces, while gray is the sum. (B) Free energy landscape of VDAC motions as determined by time-lagged independent correlation analysis. Axes are the mean-subtracted dominant principal components for the set of barrel diameters (D_{PC}) and the set of axial positions of charged residues ($z_{charged}$). (C) Molecular representation of conformational dynamics in the β-barrel and N-terminal domains of VDAC1 channel, with selected residues exhibiting large conformational plasticity labeled. Three representative frames for representative structures from states S1, S2 and S4 of VDAC1 identified in B are shown in gold, magenta, and blue ribbon representations, respectively. (D) Root-mean-square fluctuations by residue for each state identified in (B).

relative to the cytosolic side of the channel. Because the rate of VDAC closure increases with transmembrane potential, this value was chosen to be higher than typical experimental values to improve substate sampling but below the threshold at which electroporation of the membrane or deleterious effects on the VDAC structure are experimentally observed [38]. Parallel simulations comprised four independent runs ranging from 5 to 12 μs in length using ANTON2. The time evolution of the current (see Methods) of each simulation at 160 mV is shown in Figure 1A. In each independent simulation, the conductance converged to various values between 5.3 nS and 5.9 nS for T=315 K; both the current histograms (Figure 1A) and the time-averaged currents (Figure S2) suggest the presence of multiple substates differing by about 10 % in conductance. Transitions between these substates occur at μs time scales at 160 mV. The average conductance is in good agreement with single-channel electrophysiological data obtained at 37 °C [39] and with previously reported MD studies [29, 40-41]. Analysis of MD simulations showed significant flexibility of the barrel but indicated no β-barrel collapse [30], nor did the N-terminal domain leave the barrel pore in response to the voltage at either polarity [30, 42]. In total, none of the simulated ion currents showed large, persistent excursions from the average value that could be specifically identified as a gating transition such as those observed in electrophysiology experiments [1, 9-10, 28, 31].

To identify the structural basis for the channel substates, we analyzed the principal fluctuation modes of the channel by performing Markov state analysis over the entire conformational space sampled by the ≈ 40 μs of independent all-atom MD simulations collected for mVDAC1 at 160 mV. Time-lagged independent component analysis (TICA) was used to analyze the slowest principal components involved in transitions between structural states. TICA was performed independently on two sets of variables corresponding to barrel diameters (the distances between all pairs of residues within an axial distance of 5 Å from the

membrane center, as described in the Methods), and the axial (z) coordinates of all 61 VDAC charged residues. The dominant principal components for each variable set are labeled D_{PC} and $z_{charged}$, respectively. The projection of the 2D free energy surfaces onto these components is shown in Figure 1B. The free-energy surface indicates the presence of at least 4 stable conformational states, labeled S1 to S4. Molecular illustrations of representative structures for S1, S2 and S4 are shown in Figure 1C. As best as can be estimated from the sampling level achieved in the simulations, the free energy barriers between the states are relatively small, on the order of 3 to 5 k_BT, in good accord with recent estimates based on measurements of the temperature-dependence of VDAC conductance [39].

Analysis of the per-residue fluctuations (Figure 1D) suggests that residues located inside the barrel and in the loops exhibit significant, state-dependent structural flexibility. Per-residue correlation analysis reveals that, of the charged residues in the VDAC lumen, the axial position of K12 correlates most strongly with $z_{charged}$ (Table S1, Figure S3) and is thus a robust marker for the states shown in Figure 1B. (Residue E73 is outside the pore lumen and has previously been shown to have no effect on VDAC gating [43].)The transition from state S1 to state S4, for example, can be clearly marked by the vertical displacement of K12, as illustrated in Figure 1C.

Thermal noise accounts for most of the fluctuations in the simulated currents. To reduce the effects of thermal noise, we performed independent calculations on structures chosen from each of the four states identified in the free-energy landscape shown in Figure 1C. Following the protocol developed by Im and colleagues [44], we extracted 600 structures from the MD simulations with positive voltage, 150 from each of the four states, and performed Brownian dynamics (BD) simulations on each structure using the BROMOC protocol with effective interaction potentials [45]. During the BD simulations, these structures are fixed, allowing examinations of fixed electrostatic fields caused by the channel pore to ionic flows. The BD-computed currents showed conductance spanning a large range, from 4.2 to 6.6 nS; the average state-dependent conductance varied by about 10 % from state S1 (5.2 nS) to state S4 (5.7 nS) (Figure 2A). Each state was, on average, weakly anion selective (Figure 2B), with higher-conducting states also having higher anion selectivity. This suggests that higher-conducting states may have electrostatic fields more suitable to the flows of anions than cations.

Additionally, to better understand the correlation between the VDAC structure and formation of a low-conductance state, we calculated correlation coefficients between the BD-estimated conductance and the distance of the center of mass position of each residue in VDAC from the pore axis. The correlation coefficients are expressed by the color scales in Figure 2C. A magenta (cyan) color indicates a residue that strongly increases (decreases) the conductance as it moves radially away from the pore axis. While Figure 2C should not be interpreted as depicting molecular motions, it suggests that a compression of the distance between the N-terminal helix and the opposite wall is correlated to a decrease in conductance.

Similarly, the correlation between the axial position of each residue and the BD-estimated conductance is shown in Figure 2D. Here, a magenta (cyan) color denotes a residue that strongly decreases (increases) the conductance when moving in the negative z direction. The axial positions of K12 and some of the channel loops dominate the effect on channel conductance. The conductance modulation thus results from collective motions, involving changes in the positions of *both* charged residues in the N-terminus

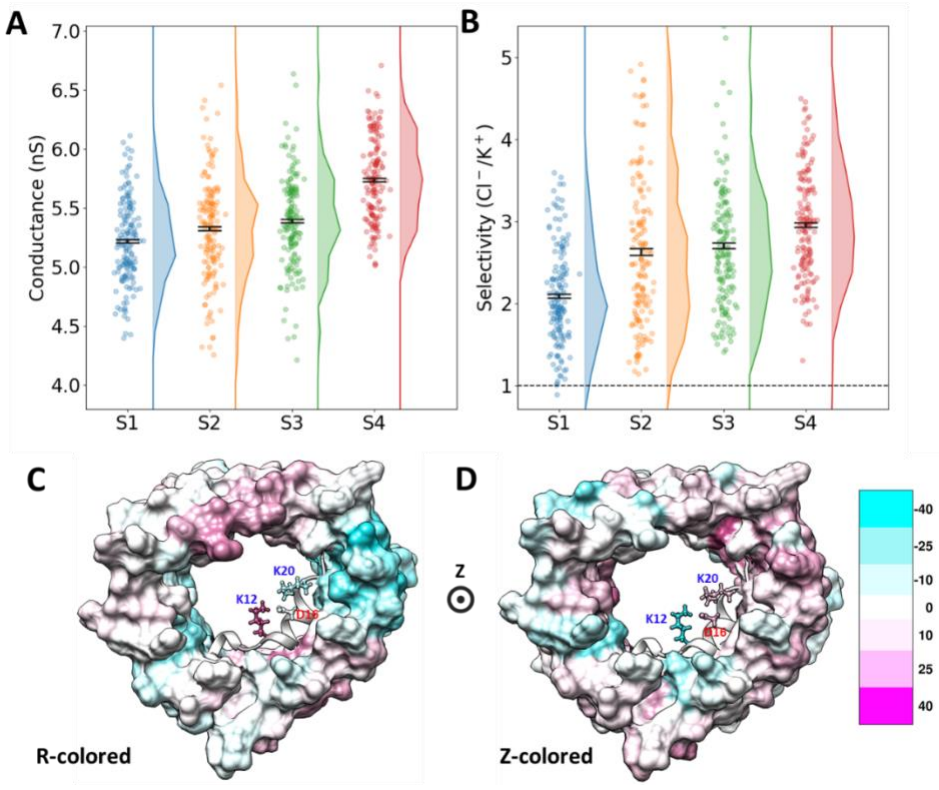

Figure 2. Summary of BD simulations of WT VDAC1. Brownian dynamics simulations of 600 randomly selected structures, 150 from each state. (A) Conductance distributions. Horizontal lines show mean values with the 68% confidence interval of the mean value. (B) Selectivity distributions. (C-D) Color maps of the residue motions that are most strongly correlated to the conductance, as determined by the correlation coefficient between the residue radial (C) or axial (D) distance from the center of mass. The magenta (cyan) color denotes a positive (negative) correlation, i.e. the conductance increases (decreases) with an increase in the corresponding coordinate. K12 is clearly identified as the residue whose motions are most strongly correlated with the channel conductance.

and those located in the barrel or loops.

Residue-level correlations between the conductance and the principal fluctuation modes determined by partial least squares regression (see the Supplemental Methods) are shown in Figure S4. This method compares the entire space of radial and axial coordinates to the BD-estimated conductance and confirms the more intuitive results shown in Figure 2C-D, especially the role of K12.

In total, the simulations reveal a mechanical coupling between the cross-section of the VDAC channel pore and the motions of charged residues, especially K12. This suggests a mechanism by which a transmembrane electric field might act on VDAC's charged residues that is coupled with barrel deformation, thus potentially driving changes in channel conductance. Restricting the motion of these charged residues is thus expected to significantly alter the channel gating. We further precisely demonstrate this effect experimentally by performing mutations on K12.

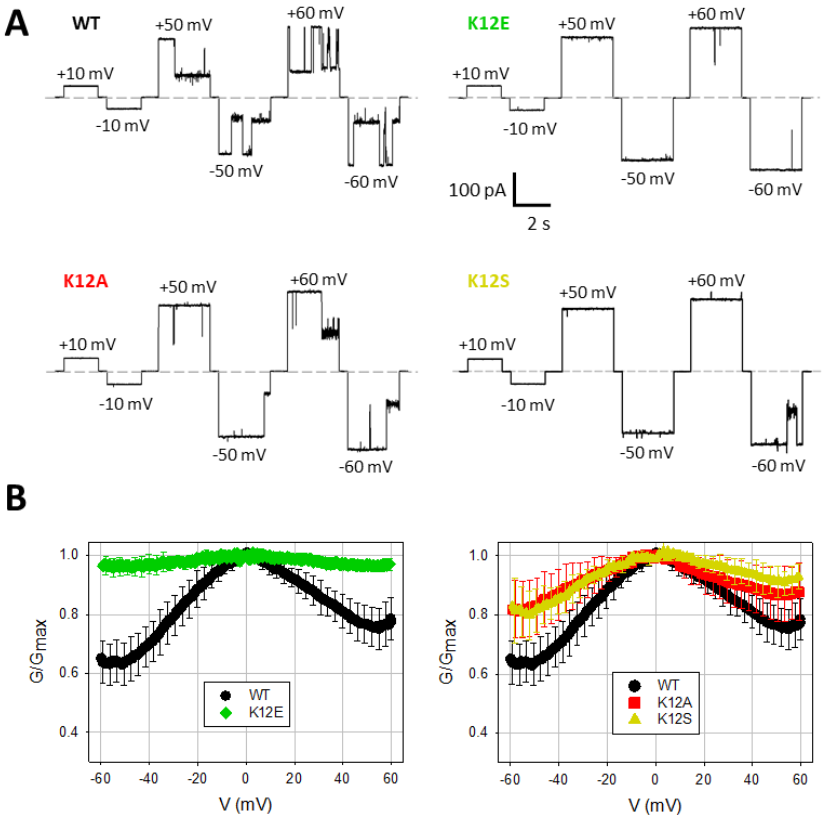

Figure 3. Gating behavior of VDAC constructs with various mutations at residue 12. (A) Current recordings from single VDAC channels show that gating is significantly suppressed in mutants relative to the wild type, with the strongest suppression occurring with the charge-reversed mutant K12E. Dashed lines indicate zero current level. Recordings were digitally filtered at 500 Hz using a low pass Bessel (8-pole) filter. (B) Quantification of gating on a multichannel system by the normalized average conductance as function of the applied voltage, showing the reduction in gating with the charge-reversed residue 12 mutant (left) and the constructs with a neutralized residue 12 (right). Data are means of 14 (WT), 6 (K12E), 5 (K12A) and 4 (K12S) independent experiments ± S.D. Error bars are shown every five points for clarity.

Mutations of K12 lead to reduced VDAC voltage gating

To interrogate the role of K12 in ion transport through VDAC in reconstitution experiments, we engineered three mVDAC1 mutants in which the positive lysine was replaced with a negatively charged glutamic acid (K12E), a hydrophobic alanine (K12A) or a polar neutral serine (K12S) residue and explored the effect of the mutations on the single-channel conductance, ionic selectivity, and voltage-gating properties of VDACs in planar lipid membranes.

Representative single channel current traces obtained with four mVDAC1 constructs—WT, K12E, K12A, and K12S— are shown in Figure 3A. All constructs exhibit the open state conductance of 4.0 ± 0.2 nS in 1M KCl at room temperature as is typical for wild type VDAC [28]. However, at increased applied voltages (±50, ±60 mV), where the WT gating characterized by random transitions between high and low conducting states is pronounced, the gating of mutants is visibly diminished, with K12E exhibiting virtually no gating, even at ± 60 mV (Figure 3A).

Given the stochastic nature of VDAC voltage gating [37, 46-47], a consistent statistical analysis of multiple channels is required for the accurate quantification of gating parameters [48-50]. The normalized conductance plots versus applied voltages obtained in multichannel experiments with mVDAC1 WT and K12 mutants are shown in Figure 3B. While the WT displays the characteristic bell-shaped voltage dependence of the normalized conductance (black symbols) for the given experimental conditions (lipid composition and salt concentration), the K12E mutant essentially does not gate, i.e., its conductance is nearly independent of voltage (green symbols). Under this experimental protocol, gating is manifested by a decrease of minimum conductance G_{min} at V > |50| mV. A slight but significant asymmetry of G_{min} observed at different polarities is another characteristic of VDAC gating [43, 48-49, 51-52]. The most pronounced difference among G_{min} (aka gating) for the four VDACs is observed at negative polarities, where the K12A and K12S mutants gate less than WT but more than K12E (Figure 3B).

Notably, at high voltages of V > |70| mV, the K12E mutant gating resumes (Figure S5), suggesting that the other charged residues in VDAC assume the role of K12,

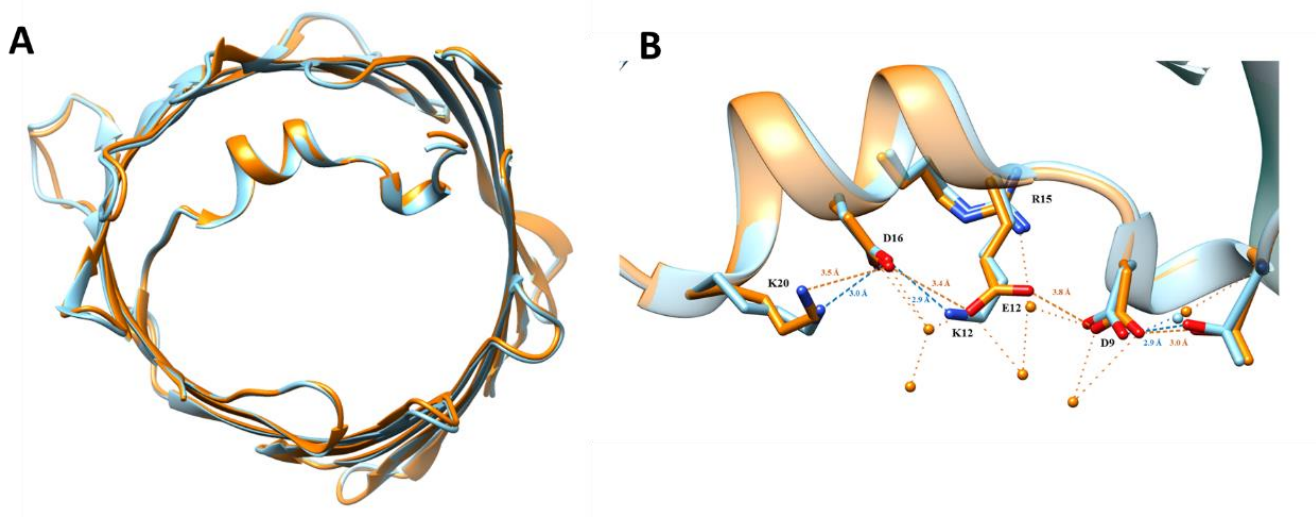

Figure 4. Crystallographic structure of K12E VDAC. **(A)** Superposed WT VDAC (in blue) and K12E VDAC (in orange) structures (top view). **(B)** Close up of the superposition of N-terminal α helix from WT VDAC1 (in blue) and K12E VDAC1 (in orange). The dotted lines denote H-bonding with water while the dashes denote intra-protein interactions. The dashes/dots and water molecules, depicted as spheres, are colored the same as the associated protein. The PDB of the K12E mutant is 7TCV.

albeit less efficiently. K12 mutations also affect VDAC ion selectivity: the selectivity of K12E is reversed to cationic, while the K12A and K12S mutants are essentially nonselective (Figure S6A); this effect is also observed in the MD simulations (Figure S6B), which identify K12 as a critical residue for VDAC voltage regulation, but not to the exclusion of other charged residues.

X-Ray Structure of K12E

The K12E mutant was crystalized in lipid bicelles in an effort to identify the structural changes resulting in the suppressed gating. Initial crystals were small and exhibited poor diffraction, but were readily optimized to achieve a resolution of 2.6 Å. The structure was resolved by molecular replacement using the wild type VDAC structure (PDB ID: 3EMN) as a search model. The TFZ and LLG values of the solution were 34 and 3476, respectively. After a few rounds of model building and structural refinement, the R_{work} and R_{free} converged to values of 22 and 27%, respectively (Table S2). The overall structure for the K12E mutant is very similar to the wild type structure, where the two structures superpose with an RMSD of 0.34 Å between the 283 aligned Cα pairs. The diameter, shape, and integrity of the K12E mutant's barrel is virtually identical to that of the WT VDAC (Figure 4A).

The N-terminal α-helix of VDAC can be subdivided into 2 portions, α1 (from residue 6 to 10) and α2 (from residue 12 to 20) with a distinctive break in alpha helical hydrogen bonding introduced by R15 sidechain. The helix has substantial interactions with water molecules and is tightly affixed to the barrel wall through multiple hydrogen bonds and hydrophobic interactions.

In the wild type structure, K12 has a lone interaction with D16 (Figure 4B), but upon mutating to Glu, the E12 sidechain forms a continuous network with the other charged residues on the helix (K20, D16, and D9). Thus, the K12E mutation appears to stabilize residue 12 via interactions with its neighboring charged residues but does not otherwise significantly alter the structure. This evidence demonstrates that the charge reversal mutation preserves the structure of VDAC while clearly suppressing the channel gating as shown in the electrophysiology data. This suggests that the structural dynamics, and not just the VDAC structure, play a critical role in determining VDAC's propensity to undergo gating transitions.

Molecular dynamics reveal a stiffer K12E mutant

To further explore how mutation of K12 affects voltage-dependent transitions in mVDAC1 without strong effects on the overall structure, all-atom simulations were performed on the VDAC-K12E mutant. Two simulations were performed, one with a starting structure from an *in silico* mutation of the WT crystallographic structure, the other from the K12E crystal structure. Both simulations were performed with the same applied electrical potential of 160 mV. The resulting current time traces are shown in Figure 5A. Both simulations which were performed for a total of ~20 μs, reached a steady conductance of ~5.6-6.5 nS, which is slightly greater than or comparable to the conductance calculated for the WT.

Figure 5B shows the results of Markov state analysis using ~20 μs of MD simulations for K12E-mVDAC1 and can be directly compared to Figure 1B. Like WT VDAC, the 2D free energy surface of the K12E mutant also indicates the presence of distinct structural states, labeled M1 to M3, but it is evident that the K12E mutation changes both the location of the states and the barriers between them. This is strikingly illustrated by the effective 1D potential of mean force (PMF) for the vertical displacement of K12 or E12 in the two constructs (Figure 5C). In WT, K12 has two stable axial positions at z = −7.5 Å and z = 5.0 Å (Figure 5C, inset), which indicate a high-amplitude bistability for K12. These stable minima for K12

are separated by a free-energy barrier of about 2.2 ± 0.5 k_BT (Figure 5C). The charge reversing mutation (K12E) also leads to two stable axial positions at z ≈ −9 Å and z ≈ −3 Å, the latter of which is between the two stable positions for K12 in WT-mVDAC1.

Similarly, in more than 40 μs of simulation comprising 10 independent trajectories at a lower temperature (300K) using the *in silico* mutated structure of K12E (Figure S8), the same states at z ≈ −3 Å and −9 Å are observed, with the z ≈ −3 Å state now being more stable. Additionally, these independent simulations show improved sampling of the PMF compared to the single long simulation (~ 17 μs in Figure 5A), in that rare excursions of residue 12 to axial positions $z > 0$ are observed. Importantly, no stable state is identified in that region. Convergence properties of the axial position distributions are explored in Figure S9A.

The two stable states in the K12E mutant are spatially closer together than those in the WT. Therefore, the free-energy profiles suggest that E12 is restricted to a narrower range of motion, at an average axial position that is between the most occupied axial positions for K12 in the WT. This restriction of E12 to an intermediate position may explain why the crystal structure of K12E is observed to be identical to the structure of WT.

The analysis of WT VDAC fluctuations suggested a mechanical coupling between residue 12 and the rest of the protein. Thus, it is expected that the reduced mobility of E12 would stiffen the mutant, reducing fluctuations throughout the molecule. This effect is shown in Figure 6A, where the root-mean-square fluctuations (RMSF) of WT and K12E constructs are directly compared. Figure 6B shows the residue-by-residue differences, demonstrating that the overall effect of the K12E mutant is to reduce the molecular fluctuations without changing the overall structure. The robustness of these results are confirmed by the independent simulations with the improved sampling (Figure S9B and Figure S10).

Further insight into the origin of the molecular stiffening can be gleaned from analysis of residue interaction networks. Networks formed among the sidechain oxygen and nitrogen atoms of the residues on the N-terminal domain and its neighboring residues were computed as described in the Methods. These were then grouped into local network communities based on time-averaged connectivity: the larger the network community

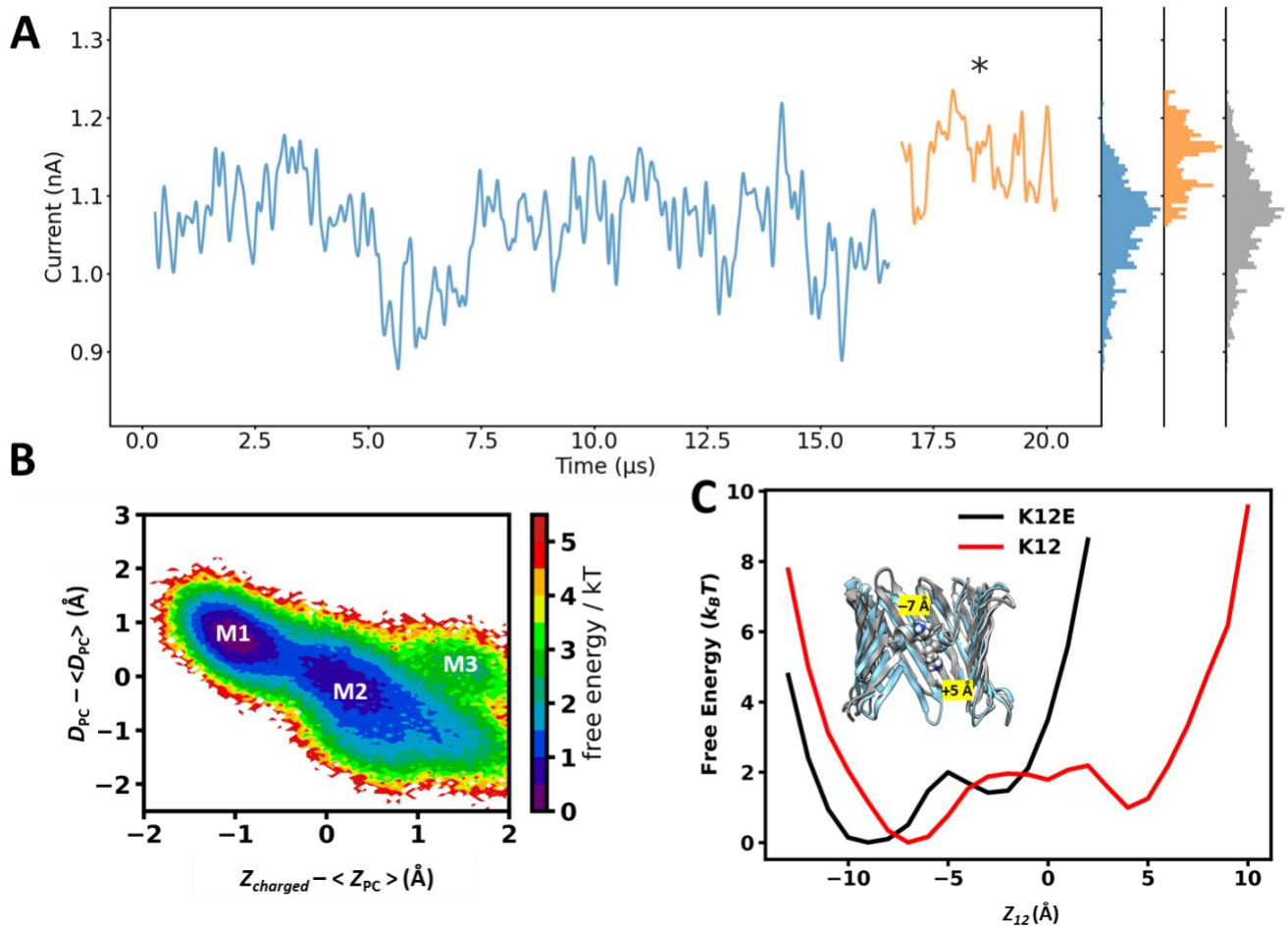

Figure 5. Atomistic MD simulations of VDAC-K12E mutant. (A) Current record of 20 μs of simulation. Instantaneous current is filtered with an 8-pole digital Bessel filter (cutoff frequency 6.9 MHz). Histograms and traces are color coded; the gray histogram is the sum of all groups. The MD simulation seeded from new X-ray structures of K12E is denoted with * and shows a similar current level to the simulation seeded from an *in silico* mutation of the WT crystallographic structure. (B) Free energy landscape of VDAC-K12E motions showing significant alterations from the WT (Fig. 1B). (C) 1D Free Energy Profile of residue 12 in the WT (K12) or mutant (K12E) along the Z-axis of the channel. The coordinate z_{12} denotes the z-coordinates of the nitrogen atom of K12 or the carbon atom of the carboxylate group of E12 , which are used to compute free-energy profiles, $F = -\log(\rho(z_{12}))$, where $\rho(z_{12})$ is the probability density. Unlike the two stable positions (inset graphic) in the WT, which occur over a broad range of z_{12}, the potential minima in the mutant are restricted to $z_{12} < 0$.

is, the more connectivity the local network has. Figure 7 shows that the entire interaction network of the WT can be grouped into 6 small interaction network communities. Community 2 is formed by S234 and the residues around K12 on the N-terminal domain. Within community 2, there is a strong correlation between K12 and S13, as indicated by the thickness of the edge connecting the sidechain oxygen atom of S13 and sidechain nitrogen atom of K12; this interaction stabilizes K12 around z = −7.5 Å. By contrast, the interaction network of K12E (Figure 7) is expanded, comprising only 4 communities. Most notably, a single large community (labeled "3") forms from the merger of WT communities 2 and 6. The E12-S13 correlation is much weaker than that of the K12-S13 pair; regardless, the expanded interaction network around E12 results in more constrained motion.

Thus, a comparison of the simulations of WT VDAC to those of the K12E mutant reveals significant alterations to the landscape of conductance substates, any of which may be a transition state in the gating pathway. State S4 (Figure 1B), which is not observed in the simulations of the K12E mutant (Figures 5B and S8A), is a candidate for such an intermediate. A definitive identification as a transition state, however, cannot be supported by the limited sampling of the simulations, which do not directly probe gating transitions and may also miss rare transition sub-states. Regardless, on the microsecond time scales accessible to simulation, we found that the K12E mutation stiffens VDAC, restraining the fluctuations of residue 12 and most other residues in the protein; we propose that this hinders exploration of conformation space and the initiation of gating transitions.

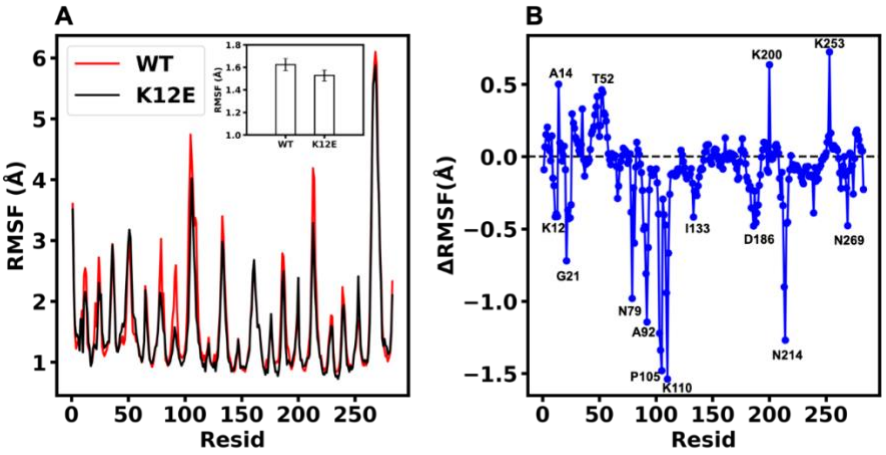

Figure 6. Simulated molecular fluctuations. (A) Root mean square fluctuations calculated for each residue in the WT and K12E mutants. The average RMSFs are shown in the inset. (B) Difference in RMSF of each residue between K12E and WT. Residue fluctuations are significantly reduced across most of the entire protein upon mutation to K12E: $\langle \Delta RMSF \rangle = -0.10 \pm 0.02$ Å.

Discussion

The corpus of experimental studies on VDAC gating highlights the striking disconnect between the complexity of VDAC gating behavior—particularly its sensitivity to mutations throughout the protein [9]—and its relatively uncomplicated structure. The gating process has clear signatures of electrostatic involvement: voltage-dependent kinetics, selectivity reversal, observed gating charge [50], pH dependence, lipid headgroup charge, electrolyte concentration dependence [43, 49, 51, 54-55]. The sensitivity of VDAC gating to its lipid environment [43, 48, 51] and to mutation of uncharged residues [10], however, also suggests a significant mechanical role of barrel dynamics and deformation in the gating process.

In the highly advanced field of potassium- and sodium-channels [56-58], the connection between transmembrane potential and mechanical motions of the channel is provided by a well-defined VSD. The VSD moves in response to applied voltages, switching the conformation of the channel between structurally distinct open and closed states that have been captured by crystallographic techniques [56-57]. By analogy, the only non-β-strand structural feature of VDAC, its α-helical N-terminal domain, was conjectured to move similarly to the VSDs of the cation channels. However, the persistence of VDAC gating after cross-linking α1 [31] or α2 (Figure S11) to the channel walls rules out motion of the N-terminal domain independent from the rest of the channel.

Similarly, previous attempts to characterize potential mechanisms of VDAC gating with molecular modelling have focused on motions of the N-terminal domain [25-26, 29-30, 41, 59]. One of the earliest molecular models explaining gating charge displacement, as well as the reduction in channel conductance and reversal of the channel selectivity upon gating, employed continuum electrostatic calculations (Poisson-Boltzmann and Poisson-Nernst-Planck) [41]. The authors critically evaluated various gating scenarios such as exit of the N-terminal domain from the channel or N-terminal rotations and translations in the trans-membrane space, concluding that none of the mechanisms proposed can be readily reconciled with the state captured in the crystal structure [7]. Zachariae and colleagues pointed out that N-terminus may be serving an important structural role, as a support beam providing sufficient mechanical rigidity to prevent the collapse of the β-barrel in response to the applied electrical field [19, 30]. Several studies used molecular simulations ranging from 100 to 1000+ ns as well as enhanced sampling techniques to show that the β-barrel is indeed very flexible, but the N-terminal domain does not leave the channel lumen, even under strong electrical fields [26, 29, 59].

In the absence of a clear VSD for VDAC, an alternative connection between transmembrane potential and the channel conductance is required. The modelling results presented in our study suggest that the electrical

transport properties of the channel are encoded not just by the N-terminal domain, but by the entire protein. Collective dynamics, which are largely governed by K12, lead to formation of distinct conductance substates, each with characteristic displacements of charged residues from the N-terminal domain in the electrical field as well as mechanically coupled changes in the pore cross-section and loop arrangements. The ~ 10 % differences in the conductance calculated for the substates is not as large as the ~ 50 % reduction in current from experimentally observed gating transitions. This suggests that the simulations probe substates of the open state conductance.

Markov State Model analysis of MD simulations, combined with the correlation analysis discussed above, have demonstrated the central role of K12 residue in VDAC transitions between sub-conductance states sampled in all-atom simulations. K12 undergoes large motions between two well-separated free energy minima, which involve modest changes in the β-barrel diameter. These observations suggest that K12 and its associated charged residues, such as K20 (Figure S12) [9], apply leverage to the barrel conformation, thus providing a link between the motion of the charged residues under the applied electric field and the barrel dynamics. The K12E mutation alters the landscape of conductance substates explored by the channel. In the mutant, residue 12 is stabilized by neighboring charged residues, resulting in restricted motion. Because of the mechanical coupling between the charged residues and the barrel conformation, restriction of residue 12 via mutation stiffens the barrel and reduces its fluctuations (Figure 6). Thus, the presence of a lysine residue at position 12 leads to a large conformational range of motion of the entire protein, enhancing VDAC's ability to explore conformational space and, presumably, to transition into gated conformations. Experimental results confirm that mutation of K12 to alanine, serine, or glutamic acid, reduces the ability of VDAC to gate (Figure 3).

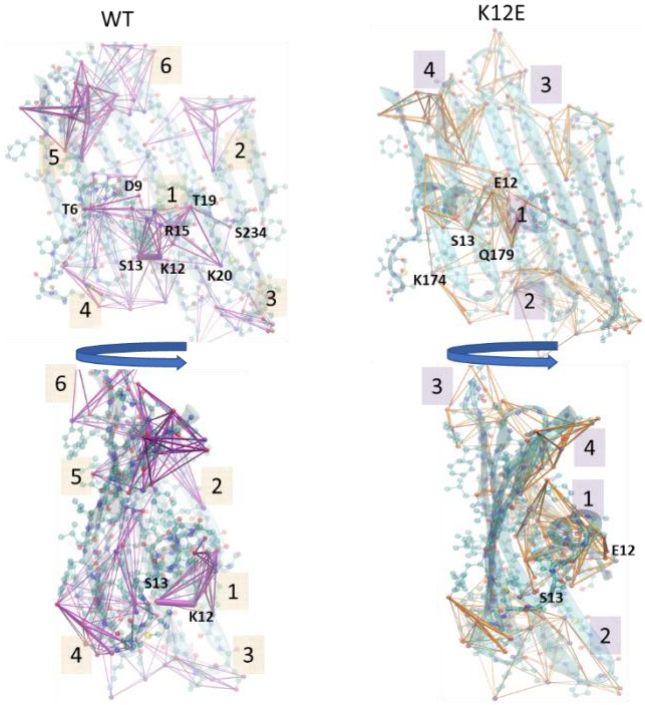

Figure 7. Interaction networks computed for WT and K12E VDAC. Networks were grouped into interaction communities labeled with numbers. Each community is identified based on time-averaged connectivity among local nodes. Edges were weighted using correlation functions computed between nodes. Graphic produced using VMD [53].

The dynamics of the VDAC barrel are thus the unifying theme. The larger the barrel fluctuations, the more readily VDAC explores the space of available conformations and finds transition states along the gating pathway. The susceptibility of the VDAC barrel to mechanical deformation determines the magnitude of its fluctuations. The susceptibility is in turn expected to be determined by two factors: the deformability of the lipid membrane, and the freedom of motion of any other protein motifs that are mechanically coupled to the barrel. This view accounts for two important experimental observations. First, residue 12 is strongly correlated to motions of the barrel; confining this residue to a smaller range of motion via the K12E mutation reduces the barrel dynamics which in turn reduces VDAC gating. Second, this mechanism accounts for the strong effect of the lipid membrane composition, which affects the membrane mechanical properties, on VDAC gating [43, 48, 51]. Future simulation and experimental studies will prove invaluable in disentangling the roles of membrane mechanics from direct chemical interactions between the highly mobile VDAC loops and the lipid headgroups.

The insight that VDAC's dynamics are collective motions of the entire protein, rather than independent motions of subdomains, illuminates two additional experimental facts. First, the multiplicity of sub-states observed in the simulation is central to understanding the departure of voltage-induced VDAC opening and closure

from two-state models. "Hidden" structural states with experimentally indistinguishable conductances provide pathways through the energy landscape that can be very different for the opening and closing processes. The existence of these was postulated based on the complex voltage-dependent VDAC gating kinetics [37] and is confirmed by the present study.

Second, we expect that the "gating charge" arises from the collective motions of all the charged residues in the channel under the applied electric field, rather than from the unidirectional motion of a single molecular domain. Colombini and coauthors, using an extensive mutagenetic analysis, identified eight charged residues that affect VDAC gating [9]. Notably, D16 and K20 are two charged residues located on the N-terminus next to K12. The crystal structure shows D16 and K20 side chains coordinating with each other (Figure 4B). The K20E mutant also reverses the selectivity to slightly cationic [60]. These mutagenetic observations support our model: the full ensemble of charged residues on the barrel wall participates in the gating process, and the contribution of some residues, especially K12, is more pronounced than others. Either of these residues can act as an independent or correlated switch to control the gating of VDAC.

The centrality of barrel dynamics in the VDAC gating process has significant implications for VDAC pharmacology. Despite an impressive list of anti-cancer drugs that were reported to target VDAC [61-62], no small-molecule compounds that meaningfully affect VDAC gating have been reported. The lack of a structurally well-defined VSD that might bind a small molecule drug accounts for this paradox and suggests that the mechanical properties of the lipid membrane and particular lipid domains in the immediate VDAC surrounding may play a more important role than specific domains of VDAC.

We note that a wide variety of structurally dissimilar β-barrel channels are observed to gate at sufficiently high potentials [15, 63-68]. Many of these occur as trimers, or have small barrel diameters, both of which provide additional mechanical stability relative to VDAC. It is thus suggestive that VDAC is both the most voltage-sensitive of these channels and has the most β-barrel flexibility. It seems likely that gating-like processes in other β-barrel channels are affected by a similar coupling between barrel compression modes and small displacements of voltage-sensitive charged residue sidechains.

Conclusion

Efforts to determine the gating mechanism of VDAC have long been plagued by the combination of the channel's deceptive simplicity and the complexity of its gating, including sensitivity to both lipid environment and electrolytic milieu. A unified view of these various experimental and computational observations follows naturally from our results. Fluctuations in the channel structure reveal the mechanical interdependence of the barrel—which is sensitive to lipidic pressure—and the motion of the charged residues, particularly K12, which are sensitive to voltage and the electrostatic environment. The structure of VDAC K12E is very similar to the WT VDAC, with no structural rearrangement of the N-terminal α-helix in the K12E mutant. The predicted impact of a K12 mutation on gating is borne out experimentally, showing that indeed it severely impairs the ability of VDAC to gate. Conversely, the presence of a lysine residue at position 12 allows relatively large-amplitude barrel fluctuations and thus enhances VDAC's ability to gate. These observations unify the results of a wealth of previous experimental and computational results regarding the gating mechanism of VDAC. They provide previously elusive avenues toward experimental control of VDAC gating and have general implications for understanding gating-like behaviors in the entire family of β-barrel channels.

Materials and Methods

Molecular dynamics (MD) simulations

The X-ray structure of mVDAC1 [PDB ID: 3EMN] [7] and K12E mutant solved in this paper were embedded in a solvated DOPC lipid bilayer using the CHARMM-GUI membrane builder [69]. The solvated protein-membrane system dimensions are 85.3 Å × 85.3 Å × 70.5 Å. The total charge of VDAC at pH7 was +3 elementary charges based on PROPKA3 calculations[70]; the ion bath contained 148 K^+ and 151 Cl^-. Excluding the volume of the bilayer, the approximate concentration was 1.1 M KCl. The CHARMM36m [71] force-field was used for protein, CHARMM36 lipid parameters for lipids [72-73], the TIP3P model for water, and CHARMM36 parameters containing NBFIX corrections for K+ and Cl^- [74-75].The protein-membrane system was equilibrated for 2.4 μs on ANTON2 platform without any applied voltage; then, the biasing voltage of 160 mV relative to the cytosolic side of the channel was applied and production simulations were run for five independent replicas extracted from the equilibrium simulations as illustrated in Figure 1A. The ANTON2 MD simulations were performed with a semi-isotropic (NPaT) ensemble at temperature 315 K both for WT and K12E systems. The multigrator scheme was used for temperature and semi-isotropic pressure coupling [76]. The time step for the production runs was set to 2 fs and trajectories were saved every 240 ps. Non-bonded and long-range electrostatic interactions were evaluated every 2 fs and 6 fs, respectively. Long-range electrostatics was calculated using the k-Gaussian Ewald method.[76-77] Seed structures of K12E mutants were derived from 10 randomly selected structures of mVDAC1 from the WT simulations; K12 was mutated to E12 using SCWRL4 [78] library as implemented in VMD [53] or states resolved with X-ray crystallography. For K12E system, a total of five starting structures were considered for 10 independent simulations using NAMD [cite: 10.1063/5.0014475] on GPU machines. The K12E seed structures were equilibrated for 2 μs without biasing voltage; the equilibrated systems were then subjected to 4-5 μs MD runs with a biasing electrical field corresponding to V=160 mV using the same protocols as for the WT simulations.

Current calculations

The instantaneous current is calculated as

$$I(t) = \frac{1}{\Delta t L_z} \sum_{all\ ions\ L} q_i[z_i(t + \Delta t) - z_i(t)] \qquad (1)$$

where Δt is the time step between saved simulation frames.

Time-lagged Independent Component Analysis (TICA)

Time-lagged Independent Component Analysis (TICA) computes autocorrelations in the dynamical data and then decomposes them in terms of their correlation strengths and eigenstates. TICA solves for eigenvalues λ_i and eigenvectors v_i of the following equation:

$$C(\tau_l)v_i = \lambda_i C(0)v_i \qquad (2)$$

where $C(\tau_l) = \langle x_m(t + \tau_l)x_l(t)\rangle$ is the covariance matrix computed from the time average between any two time-series variables $x_m(t)$ with zero means. The lagtime τ_l was set to 100 steps (or approximately 20 ns) to avoid residual memories in each time-series.

Two sets of time-series variables were chosen to highlight radial motions of barrel residues and axial motions of charged residues, and TICA was performed independently on each set of the time-series data. First, $r_{C\alpha-C\alpha}$ was defined as the set of distances projected on the xy-plane between carbon Cα atoms of the beta barrel residues (*i,j*) (for all residues *i,*j > 22, i.e., excluding the N-terminal, and $i - j > 5$, i.e., excluding neighboring residues) having $|z_{C\alpha}| <= 5$ Å with respect to the center of mass of the VDAC beta barrel. The second set, z_{KRED}, comprised the axial (z) positions of all 61 charged residues.

The first component of the TICA space is a principal component with zero mean, which possesses the largest value of λ_i (corresponding to the slowest time scale). Only the first component was used for subsequent analysis. Note that the sign of the first components can be arbitrary from the TICA analysis because TICA was performed on zero-mean data. The sign of the first component (denoted as D_{PC}) obtained from $r_{C\alpha-C\alpha}$ was taken to produce a positive correlation with the change in distance between two residues, 23 and 99, that are located at opposite sides of the barrel. The sign of the first component (denoted as $z_{charged}$) obtained from z_{KRED} was determined by requiring a positive correlation with the axial motion of K12.

Root mean square fluctuation

To quantify a structural flexibility, we computed the root mean square fluctuation (RMSF) as follows,

$$RMSF_i = (N_i)^{-1} \sum_{j=1}^{N_i} \sqrt{(x_i(t_j) - \langle x_i\rangle)^2 + (y_i(t_j) - \langle y_i\rangle)^2 + (z_i(t_j) - \langle z_i\rangle)^2} \qquad (3)$$

where i is an index of a Carbon-alpha atom, N_i is a number of frames, $x_i(t_j)$, $y_i(t_j)$ and $z_i(t_j)$ are coordinates at time t_j after a structure alignment with the average structure defined by $\langle x_i\rangle, \langle y_i\rangle$ and $\langle z_i\rangle$, which are averages of $x(t_j), z(t_j)$, and $z(t_j)$, respectively.

Interaction Network Analysis

To differentiate the dynamical networks of interactions in VDAC-WT and K12E, we used the *NetworkView* method [79] implemented in VMD [53]. We selected the oxygen and nitrogen atoms of residues 1-21 and 166 to 246 as nodes. Edges between nodes on different residues were computed within a cutoff distance (4.5 Å) for at least 75% of a time-accumulated MD trajectory. Pairs of atoms on the same residues were excluded. The edge thickness d_{ij} between two nodes i and j was computed from pairwise correlation function C_{ij}, namely, $d_{ij} = -\log(|C_{ij}|)$, where

$$C_{ij} = \frac{\langle \Delta\vec{r}_i(t)\Delta\vec{r}_j(t)\rangle}{\sqrt{\langle \Delta\vec{r}_i(t)^2\rangle\langle \Delta\vec{r}_j(t)^2\rangle}} \qquad (4)$$

where $\Delta\vec{r}_i(t) = \vec{r}_i(t) - \langle\vec{r}_i(t)\rangle$, $\vec{r}_i(t)$ is the position of the *i*-th node, and brackets indicate time averaging. The networks were then grouped based on the time averaged connectivity of the nodes using the Girvan-Newman algorithm [80].

Brownian Dynamics Simulations

To evaluate per-state conductance, we performed ensemble of the Grand-Canonical Monte-Carlo/Brownian Dynamics simulations on 600 structures, 150 from each of the four states derived from the TICA analysis. The GCMC/BD runs were carried out with the BROMOC program suite[45] with the set of effective pairwise ion-ion interactions potentials developed previously. Each structure was re-oriented relative to the state resolved in X-ray structure. The nanopore and dielectric boundaries were represented by a combination of a static field, membrane potential (obtained from the solution of the Poisson-Boltzmann equation), and repulsive potential and reaction field terms. The rigid protein with a dielectric constant of $\varepsilon_p = 2$ was solvated in implicit water ($\varepsilon_w = 80$). A cylinder with R=15 Å, dielectric constant of $\varepsilon_c = 80$, and length of 32 Å was added to represent the permeation pathway inside the VDAC pore[44]. The radius of the cylinder is slightly greater that the radius of the largest cross-section in VDAC to encompass the entire accessible permeation volume. The protein was embedded into an explicit lipid bilayer ($\varepsilon_b = 2$) with a thickness of $T_m = 32$ Å at the position z = 0.0.[44] All atomic charges in the bilayer were set to zero and the default CHARMM36 van-der-Waals radii were used to create a repulsive, low-dielectric environment and to ensure lack of permeation outside of the VDAC pore. A rectangular periodic box of size 68.5 Å × 68.5 Å × 62.5 Å was used for all BD simulations. The salt (KCl) concentration was kept at 1.0 M with two symmetric 3.0 Å buffers from 31.25 Å to 28.25 Å and from −31.25 Å to −28.25 Å. The applied external electric potential was set to +160 mV to match

the polarity used in the MD simulations used for clustering. Five GCMC-BD runs were performed for each structure, using different seed numbers to generate the initial ion distribution, with a production time of 2 micro-seconds.

Protein production and purification

Recombinant murine VDAC1 wild-type and mutants were expressed and purified as described previously for wild-type [7]. Refolded proteins were injected on a size exclusion chromatography column (Superdex 200, GE healthcare) in 150 mM NaCl, 20 mM Tris-HCl pH 8.0, 0.1% LDAO and the refolded peak was used for functional studies.

VDAC reconstitution and conductance measurements

Planar lipid membranes were formed by apposition of two monolayers of soybean Polar Lipid Extract (PLE) in pentane (Avanti Polar Lipids, Alabaster, AL) across an ~70-µm aperture in the 15-µm-thick Teflon partition that separates two ~1.5-ml compartments filed with 1 M KCl solutions buffered by 5 mM HEPES at pH 7.4, as previously described [81].Channel insertion was achieved by adding 0.1–2 µl of VDAC diluted to a final concentration of 20-50 ng/µL in buffer containing 100 mM Tris, 50 mM KCl, 1 mM EDTA, 15% (v/v) DMSO, 2.5% (v/v) Triton X-100, pH 7.35 to the membrane bathing solution while stirring. Potential was defined as positive when it was greater at the side of VDAC addition (cis side). Current recordings were performed as described previously [81] using an Axopatch 200B amplifier (Molecular Devices, LLC) in the voltage-clamp mode. Single-channel data were filtered by a low pass 8-pole Butterworth filter (Model 900 Frequency Active Filter, Frequency Devices, Inc.) at 15 kHz and saved with a sampling frequency of 50 kHz and analyzed using pClamp 10.7 software (Molecular Devices, LLC).

VDAC voltage gating was measured following a protocol previously devised [28, 48-49]. Gating properties were inferred from the channels response to a slow symmetrical 5 mHz triangular voltage wave of ±60 mV amplitude from an Arbitrary Waveform Generator 33220A (Agilent Technologies). Data were acquired at a sampling frequency of 2 Hz and analyzed as described previously [48-49] using pClamp 10.7 software and an algorithm developed in-house [37].

Selectivity experiments were carried out in 1 M (cis) versus 0.2 M KCl (trans) gradient, buffered with 5 mM HEPES at pH 7.4, as described previously [49]. VDAC ion selectivity was inferred by measuring the reversal potential, which is the applied voltage needed to cancel the current observed when one or several selective ion channels insert under a concentration gradient. The measured reversal potential was corrected by the liquid junction potential calculated from Henderson's equation [82] to obtain the final reversal potential, which was used to calculate permeability ratios between K^+ and Cl^-, P_{Cl^-}/P_{K^+}, according to the Goldman-Hodgkin-Katz equation [83].

Crystallization and structure solution of VDAC1 K12E

For crystallization, K12E-mVDAC1 was purified in a buffer containing 20 mM Tris HCl, pH 8.5, 50 mM NaCl and 0.1% LDAO. The crystallization was carried out in bicelles using the hanging-drop vapor diffusion method. 15 mg/mL of purified protein was mixed with a 35% 1,2-dimyristoyl-sn-glycero-3-phosphocholine (DMPC) and 3-([3-Cholamidopropyl]dimethylammonio)-2-hydroxy-1-propanesulfonate (CHAPSO) bicelle solution in a 4:1 ratio. The final concentration of VDAC used for crystallization was 12 mg/ml in a 7% bicelle solution. This protein-bicelle mixture was set up for crystallization at 20° C in conditions with 0.1 M Tris-HCl, pH 8.5, 10% (Polyethylene glycol) PEG 400 and 15% to 20% concentration gradient of 2-Methyl-2,4-pentanediol (MPD). The crystals were harvested after 14 days and used for data collection at the beamline 5.0.1 at the Advanced Light Source (Berkeley, CA). The data was integrated using XDS [84-85] and scaled using Aimless [86-87]. The structure solution was obtained by molecular replacement carried out by Phaser [88] using WT mVDAC1 as a template (PDB ID: 3EMN). Model building and refinement was carried out using Coot [89] and Refmac [90-91], respectively. The structure illustrations were generated using Chimera [92].

ASSOCIATED CONTENT

Supporting Information. Supplemental methods for correlation analysis, partial least squares regression analysis, and time-averaged current calculation. Supplemental tables of ranked correlation between residue coordinates and data collection and refinement statistics for diffraction from crystals of VDAC-K12E. 10 supplemental figures. This material is available free of charge via the Internet at http://pubs.acs.org.

AUTHOR INFORMATION

Corresponding Author

* david.hoogerheide@nist.gov

Author Contributions

† These authors contributed equally.

Funding Sources

VAN acknowledges postdoctoral fellowships from Alberta Innovates-Health Solutions (AIHS, 2015-2017), Canadian Institutes of Health Research (CIHR, 2016-2018), and Los Alamos National Lab Director's Fellowship (2018-2021) for the work on VDAC. MQM, SMB, and TKR were supported by the Intramural Research Program of the National Institutes of Health, *Eunice Kennedy Shriver* National Institute of Child Health and Human Development. MQM acknowledges postdoctoral fellowship *Juan de la Cierva Incorporación* from the Spanish Ministry of Science and Innovation MCIN/AEI/ 10.13039/501100011033 (IJC2018-035283-I, 2020-2022) and support from Universitat Jaume I (project UJI-A2020-21). Anton 2 computer time was provided through allocation PSCA16049P to DPH and SYN by the Pittsburgh

Supercomputing Center (PSC) through Grant R01GM116961 from the National Institutes of Health.

ACKNOWLEDGMENT

This work was initiated and led by, and is dedicated to the memory of, Sergei Noskov. The Anton 2 machine at PSC was generously made available by D.E. Shaw Research. Certain commercial materials, equipment, and instruments are identified in this work to describe the experimental procedure as completely as possible. In no case does such an identification imply a recommendation or endorsement by NIST, nor does it imply that the materials, equipment, or instruments identified are necessarily the best available for the purpose.

ABBREVIATIONS

VDAC, voltage-dependent anion channel; ATP, adenosine triphosphate; ADP, adenosine diphosphate; MOM, mitochondrial outer membrane; MD, molecular dynamics; WT, wild type; VSD, voltage-sensing domain; TICA, time-lagged independent component analysis; BD, Brownian dynamics;

REFERENCES

1. Colombini, M., VDAC: The channel at the interface between mitochondria and the cytosol. *Mol Cell Biochem* **2004,** *256* (1-2), 107-115.
2. Lemasters, J. J.; Holmuhamedov, E., Voltage-dependent anion channel (VDAC) as mitochondrial governator--thinking outside the box. *Biochimica et biophysica acta* **2006,** *1762* (2), 181-90.
3. Colombini, M., Pore-Size and Properties of Channels from Mitochondria Isolated from Neurospora-Crassa. *J Membrane Biol* **1980,** *53* (2), 79-84.
4. Gurnev, P. A.; Rostovtseva, T. K.; Bezrukov, S. M., Tubulin-blocked state of VDAC studied by polymer and ATP partitioning. *FEBS Letters* **2011,** *585* (14), 2363-2366.
5. Bayrhuber, M.; Meins, T.; Habeck, M.; Becker, S.; Giller, K.; Villinger, S.; Vonrhein, C.; Griesinger, C.; Zweckstetter, M.; Zeth, K., Structure of the human voltage-dependent anion channel. *Proceedings of the National Academy of Sciences* **2008,** *105* (40), 15370-15375.
6. Hiller, S.; Garces, R. G.; Malia, T. J.; Orekhov, V. Y.; Colombini, M.; Wagner, G., Solution Structure of the Integral Human Membrane Protein VDAC-1 in Detergent Micelles. *Science* **2008,** *321* (5893), 1206.
7. Ujwal, R.; Cascio, D.; Colletier, J. P.; Faham, S.; Zhang, J.; Toro, L.; Ping, P. P.; Abramson, J., The crystal structure of mouse VDAC1 at 2.3 angstrom resolution reveals mechanistic insights into metabolite gating. *Proc Natl Acad Sci USA* **2008,** *105* (46), 17742-17747.
8. Song, J.; Midson, C.; Blachly-Dyson, E.; Forte, M.; Colombini, M., The Topology of VDAC as Probed by Biotin Modification. *J Biol Chem* **1998,** *273* (38), 24406-24413.
9. Thomas, L.; Blachly-Dyson, E.; Colombini, M.; Forte, M., Mapping of residues forming the voltage sensor of the voltage-dependent anion-selective channel. *Proceedings of the National Academy of Sciences* **1993,** *90* (12), 5446-5449.
10. Song, J. M.; Midson, C.; Blachly-Dyson, E.; Forte, M.; Colombini, M., The sensor regions of VDAC are translocated from within the membrane to the surface during the gating processes. *Biophys J* **1998,** *74* (6), 2926-2944.
11. Rostovtseva, T.; Colombini, M., ATP flux is controlled by a voltage-gated channel from the mitochondrial outer membrane. *J Biol Chem* **1996,** *271* (45), 28006-8.
12. Noskov, S. Y.; Rostovtseva, T. K.; Bezrukov, S. M., ATP Transport through VDAC and the VDAC-Tubulin Complex Probed by Equilibrium and Nonequilibrium MD Simulations. *Biochemistry-Us* **2013,** *52* (51), 9246-9256.
13. Hodge, T.; Colombini, M., Regulation of metabolite flux through voltage-gating of VDAC channels. *J Membr Biol* **1997,** *157* (3), 271-9.
14. Tan, W.; Colombini, M., VDAC closure increases calcium ion flux. *Biochimica et biophysica acta* **2007,** *1768* (10), 2510-5.
15. Perini, D.; Alcaraz, A.; Queralt-Martín, M., Lipid Headgroup Charge and Acyl Chain Composition Modulate Closure of Bacterial β-Barrel Channels. *International Journal of Molecular Sciences* **2019,** *20* (3), 674.
16. Blaustein, R. O.; Lea, E. J.; Finkelstein, A., Voltage-dependent block of anthrax toxin channels in planar phospholipid bilayer membranes by symmetric tetraalkylammonium ions. Single-channel analysis. *Journal of General Physiology* **1990,** *96* (5), 921-942.
17. Wilmsen, H. U.; Pattus, F.; Buckley, J. T., Aerolysin, a hemolysin fromAeromonas hydrophila, forms voltage-gated channels in planar lipid bilayers. *The Journal of Membrane Biology* **1990,** *115* (1), 71-81.
18. Korchev, Y. E.; Alder, G. M.; Bakhramov, A.; Bashford, C. L.; Joomun, B. S.; Sviderskaya, E. V.; Usherwood, P. N. R.; Pasternak, C. A., Staphylococcus aureus alpha-toxin-induced pores: Channel-like behavior in lipid bilayers and patch clamped cells. *The Journal of Membrane Biology* **1995,** *143* (2), 143-151.
19. Böhm, R.; Amodeo, G. F.; Murlidaran, S.; Chavali, S.; Wagner, G.; Winterhalter, M.; Brannigan, G.; Hiller, S., The Structural Basis for Low Conductance in the Membrane Protein VDAC upon β-NADH Binding and Voltage Gating. *Structure* **2020,** *28* (2), 206-214.e4.
20. Martynowycz, M. W.; Khan, F.; Hattne, J.; Abramson, J.; Gonen, T., MicroED structure of lipid-embedded mammalian mitochondrial voltage-dependent anion channel. *Proceedings of the National Academy of Sciences* **2020,** *117* (51), 32380-32385.
21. Choudhary, O. P.; Paz, A.; Adelman, J. L.; Colletier, J.-P.; Abramson, J.; Grabe, M., Structure-guided simulations illuminate the mechanism of ATP transport through VDAC1. *Nature Structural & Molecular Biology* **2014,** *21* (7), 626-632.
22. Hiller, S.; Abramson, J.; Mannella, C.; Wagner, G.; Zeth, K., The 3D structures of VDAC represent a native conformation. *Trends Biochem Sci* **2010,** *35* (9), 514-21.
23. Long, S. B.; Campbell, E. B.; MacKinnon, R., Voltage Sensor of Kv1.2: Structural Basis of Electromechanical Coupling. *Science* **2005,** *309* (5736), 903-908.
24. Colombini, M.; Blachly-Dyson, E.; Forte, M., VDAC, a channel in the outer mitochondrial membrane. *Ion Channels* **1996,** *4*, 169-202.
25. Preto, J.; Gorny, H.; Krimm, I., A Deep Dive into VDAC1 Conformational Diversity Using All-Atom Simulations Provides New Insights into the Structural Origin of the Closed States. *International Journal of Molecular Sciences* **2022,** *23* (3), 1175.
26. Preto, J.; Krimm, I., The intrinsically disordered N-terminus of the voltage-dependent anion channel. *Plos Comput Biol* **2021,** *17* (2), e1008750.
27. Zimmerberg, J.; Parsegian, V. A., Polymer Inaccessible Volume Changes during Opening and Closing of a Voltage-Dependent Ionic Channel. *Nature* **1986,** *323* (6083), 36-39.
28. Colombini, M., Voltage gating in the mitochondrial channel, VDAC. *The Journal of Membrane Biology* **1989,** *111* (2), 103-111.

29. Villinger, S.; Briones, R.; Giller, K.; Zachariae, U.; Lange, A.; De Groot, B. L.; Griesinger, C.; Becker, S.; Zweckstetter, M., Functional dynamics in the voltage-dependent anion channel. *Proceedings of the National Academy of Sciences* **2010,** *107* (52), 22546-22551.

30. Zachariae, U.; Schneider, R.; Briones, R.; Gattin, Z.; Demers, J.-P.; Giller, K.; Maier, E.; Zweckstetter, M.; Griesinger, C.; Becker, S.; Benz, R.; Groot, D., L., Bert; Lange, A., β-Barrel Mobility Underlies Closure of the Voltage-Dependent Anion Channel. *Structure* **2012,** *20* (9), 1540-1549.

31. Teijido, O.; Ujwal, R.; Hillerdal, C.-O.; Kullman, L.; Rostovtseva, T. K.; Abramson, J., Affixing N-terminal α-Helix to the Wall of the Voltage-dependent Anion Channel Does Not Prevent Its Voltage Gating. *J Biol Chem* **2012,** *287* (14), 11437-11445.

32. Briones, R.; Weichbrodt, C.; Paltrinieri, L.; Mey, I.; Villinger, S.; Giller, K.; Lange, A.; Zweckstetter, M.; Griesinger, C.; Becker, S.; Steinem, C.; Groot, D., L., Bert, Voltage Dependence of Conformational Dynamics and Subconducting States of VDAC-1. *Biophys J* **2016,** *111* (6), 1223-1234.

33. Ge, L.; Villinger, S.; Mari, A., Stefania; Giller, K.; Griesinger, C.; Becker, S.; Müller, J., Daniel; Zweckstetter, M., Molecular Plasticity of the Human Voltage-Dependent Anion Channel Embedded Into a Membrane. *Structure* **2016,** *24* (4), 585-594.

34. Reif, M. M.; Fischer, M.; Fredriksson, K.; Hagn, F.; Zacharias, M., The N-Terminal Segment of the Voltage-Dependent Anion Channel: A Possible Membrane-Bound Intermediate in Pore Unbinding. *J Mol Biol* **2019,** *431* (2), 223-243.

35. Rostovtseva, T. K.; Tan, W. Z.; Colombini, M., On the role of VDAC in apoptosis: Fact and fiction. *J Bioenerg Biomembr* **2005,** *37* (3), 129-142.

36. Rostovtseva, T. K.; Bezrukov, S. M., VDAC inhibition by tubulin and its physiological implications. *Biochim Biophys Acta - Biomembranes* **2012,** *1818* (6), 1526-1535.

37. Rappaport, S. M.; Teijido, O.; Hoogerheide, D. P.; Rostovtseva, T. K.; Berezhkovskii, A. M.; Bezrukov, S. M., Conductance hysteresis in the voltage-dependent anion channel. *Eur Biophys J Biophy* **2015,** *44* (6), 465-472.

38. Kotnik, T.; Rems, L.; Tarek, M.; Miklavčič, D., Membrane Electroporation and Electropermeabilization: Mechanisms and Models. *Annual Review of Biophysics* **2019,** *48* (1), 63-91.

39. Queralt-Martín, M.; Hoogerheide, D. P.; Noskov, S. Y.; Berezhkovskii, A. M.; Rostovtseva, T. K.; Bezrukov, S. M., VDAC Gating Thermodynamics, but Not Gating Kinetics, Are Virtually Temperature Independent. *Biophys J* **2020,** *119* (12), 2584-2592.

40. Rui, H.; Lee, K. I.; Pastor, R. W.; Im, W., Molecular Dynamics Studies of Ion Permeation in VDAC. *Biophys J* **2011,** *100* (3), 602-610.

41. Choudhary, O. P.; Ujwal, R.; Kowallis, W.; Coalson, R.; Abramson, J.; Grabe, M., The Electrostatics of VDAC: Implications for Selectivity and Gating. *J Mol Biol* **2010,** *396* (3), 580-592.

42. Mertins, B.; Psakis, G.; Grosse, W.; Back, K. C.; Salisowski, A.; Reiss, P.; Koert, U.; Essen, L. O., Flexibility of the N-terminal mVDAC1 segment controls the channel's gating behavior. *PLoS One* **2012,** *7* (10), e47938.

43. Queralt-Martín, M.; Bergdoll, L.; Jacobs, D.; Bezrukov, S. M.; Abramson, J.; Rostovtseva, T. K., Assessing the role of residue E73 and lipid headgroup charge in VDAC1 voltage gating. *Biochim Biophys Acta - Bioenergetics* **2019,** *1860* (1), 22-29.

44. Lee, K. I.; Rui, H.; Pastor, R. W.; Im, W., Brownian dynamics simulations of ion transport through the VDAC. *Biophys J* **2011,** *100* (3), 611-619.

45. De Biase, P. M.; Markosyan, S.; Noskov, S., BROMOC suite: Monte Carlo/Brownian dynamics suite for studies of ion permeation and DNA transport in biological and artificial pores with effective potentials. *J Comput Chem* **2015,** *36* (4), 264-71.

46. Banerjee, K., Dynamic memory of a single voltage-gated potassium ion channel: A stochastic nonequilibrium thermodynamic analysis. *The Journal of Chemical Physics* **2015,** *142* (18), 185101.

47. Pustovoit, M. A.; Berezhkovskii, A. M.; Bezrukov, S. M., Analytical theory of hysteresis in ion channels: Two-state model. *The Journal of Chemical Physics* **2006,** *125* (19), 194907.

48. Rostovtseva, T. K.; Kazemi, N.; Weinrich, M.; Bezrukov, S. M., Voltage gating of VDAC is regulated by nonlamellar lipids of mitochondrial membranes. *J Biol Chem* **2006,** *281* (49), 37496-506.

49. Teijido, O.; Rappaport, S. M.; Chamberlin, A.; Noskov, S. Y.; Aguilella, V. M.; Rostovtseva, T. K.; Bezrukov, S. M., Acidification asymmetrically affects voltage-dependent anion channel implicating the involvement of salt bridges. *J Biol Chem* **2014,** *289* (34), 23670-82.

50. Colombini, M., Voltage gating in the mitochondrial channel, VDAC. *J Membr Biol* **1989,** *111* (2), 103-111.

51. Mlayeh, L.; Krammer, E.-M.; Léonetti, M.; Prévost, M.; Homblé, F., The mitochondrial VDAC of bean seeds recruits phosphatidylethanolamine lipids for its proper functioning. *Biochim Biophys Acta - Bioenergetics* **2017,** *1858* (9), 786-794.

52. Eddy, M. T.; Ong, T.-C.; Clark, L.; Teijido, O.; Van Der Wel, P. C. A.; Garces, R.; Wagner, G.; Rostovtseva, T. K.; Griffin, R. G., Lipid Dynamics and Protein–Lipid Interactions in 2D Crystals Formed with the β-Barrel Integral Membrane Protein VDAC1. *J Am Chem Soc* **2012,** *134* (14), 6375-6387.

53. Humphrey, W.; Dalke, A.; Schulten, K., VMD: visual molecular dynamics. *J Mol Graph* **1996,** *14* (1), 33-8, 27-8.

54. Bowen, K. A.; Tam, K.; Colombini, M., Evidence for titratable gating charges controlling the voltage dependence of the outer mitochondrial membrane channel, VDAC. *The Journal of Membrane Biology* **1985,** *86* (1), 51-59.

55. Mlayeh, L.; Chatkaew, S.; Léonetti, M.; Homblé, F., Modulation of Plant Mitochondrial VDAC by Phytosterols. *Biophys J* **2010,** *99* (7), 2097-2106.

56. Catterall, W. A.; Lenaeus, M. J.; Gamal El-Din, T. M., Structure and Pharmacology of Voltage-Gated Sodium and Calcium Channels. *Annu Rev Pharmacol Toxicol* **2020,** *60*, 133-154.

57. Gouaux, E.; Mackinnon, R., Principles of selective ion transport in channels and pumps. *Science* **2005,** *310* (5753), 1461-5.

58. Bezanilla, F., How membrane proteins sense voltage. *Nat Rev Mol Cell Biol* **2008,** *9* (4), 323-32.

59. Noskov, S. Y.; Rostovtseva, T. K.; Chamberlin, A. C.; Teijido, O.; Jiang, W.; Bezrukov, S. M., Current state of theoretical and experimental studies of the voltage-dependent anion channel (VDAC). *Biochimica et biophysica acta* **2016,** *1858* (7 Pt B), 1778-90.

60. Blachly-Dyson, E.; Peng, S. Z.; Colombini, M.; Forte, M., Selectivity changes in site-directed mutants of the VDAC ion channel - structural implications. *Science* **1990,** *247* (4947), 1233-1236.

61. Reina, S.; De Pinto, V., Anti-Cancer Compounds Targeted to VDAC: Potential and Perspectives. *Curr Med Chem* **2017,** *24* (40), 4447-4469.

62. Rostovtseva, T. K.; Queralt-Martin, M.; Rosencrans, W. M.; Bezrukov, S. M., Targeting the Multiple Physiologic Roles of VDAC With Steroids and Hydrophobic Drugs. *Front Physiol* **2020,** *11*, 446.

63. Delcour, A. H. Solute uptake through general porins *Front Biosci* [Online], 2003, p. d1055-71. PubMed. http://europepmc.org/abstract/MED/12700124 https://doi.org/10.2741/1132 (accessed 2003/05//).

64. Liko, I.; Degiacomi, M. T.; Lee, S.; Newport, T. D.; Gault, J.; Reading, E.; Hopper, J. T. S.; Housden, N. G.; White, P.; Colledge, M.; Sula, A.; Wallace, B. A.; Kleanthous, C.; Stansfeld, P. J.; Bayley, H.; Benesch, J. L. P.; Allison, T. M.; Robinson, C. V., Lipid binding attenuates channel closure of the outer membrane protein OmpF. *Proceedings of the National Academy of Sciences* **2018,** *115* (26), 6691-6696.

65. Nikaido, H., Molecular Basis of Bacterial Outer Membrane Permeability Revisited. *Microbiology and Molecular Biology Reviews* **2003,** *67* (4), 593-656.

66. Wager, B.; Baslé, A.; Delcour, A. H., Disulfide bond tethering of extracellular loops does not affect the closure of OmpF porin at acidic pH. *Proteins: Structure, Function, and Bioinformatics* **2010,** *78* (14), 2886-2894.

67. Larimi, M. G.; Ha, J.-H.; Loh, S. N.; Movileanu, L., Insertion state of modular protein nanopores into a membrane. *Biochimica et Biophysica Acta (BBA) - Biomembranes* **2021,** *1863* (5), 183570.

68. Vasan, A. K.; Haloi, N.; Ulrich, R. J.; Metcalf, M. E.; Wen, P.-C.; Metcalf, W. W.; Hergenrother, P. J.; Shukla, D.; Tajkhorshid, E., Investigation of gating in outer membrane porins provides new perspectives on antibiotic resistance mechanisms. Cold Spring Harbor Laboratory: 2021.

69. Jo, S.; Kim, T.; Iyer, V. G.; Im, W., CHARMM-GUI: a web-based graphical user interface for CHARMM. *J Comput Chem* **2008,** *29* (11), 1859-65.

70. Olsson, M. H.; Sondergaard, C. R.; Rostkowski, M.; Jensen, J. H., PROPKA3: Consistent Treatment of Internal and Surface Residues in Empirical pKa Predictions. *J Chem Theory Comput* **2011,** *7* (2), 525-37.

71. Huang, J.; Rauscher, S.; Nawrocki, G.; Ran, T.; Feig, M.; De Groot, B. L.; Grubmüller, H.; Mackerell, A. D., CHARMM36m: an improved force field for folded and intrinsically disordered proteins. *Nature Methods* **2017,** *14* (1), 71-73.

72. Klauda, J. B.; Venable, R. M.; Freites, J. A.; O'Connor, J. W.; Tobias, D. J.; Mondragon-Ramirez, C.; Vorobyov, I.; MacKerell, A. D.; Pastor, R. W., Update of the CHARMM All-Atom Additive Force Field for Lipids: Validation on Six Lipid Types. *J Phys Chem B* **2010,** *114* (23), 7830-7843.

73. Klauda, J.; Monje, V.; Kim, T.; Im, W., Improving the CHARMM Force Field for Polyunsaturated Fatty Acid Chains. *J Phys Chem B* **2012,** *116* (31), 9424-9431.

74. Noskov, S. Y.; Roux, B., Control of ion selectivity in LeuT: two Na+ binding sites with two different mechanisms. *J Mol Biol* **2008,** *377* (3), 804-18.

75. Jorgensen, W. L.; Chandrasekhar, J.; Madura, J. D.; Impey, R. W.; Klein, M. L., Comparison of Simple Potential Functions for Simulating Liquid Water. *J Chem Phys* **1983,** *79* (2), 926-935.

76. Shaw, D. E., Grossman, J.P., Bank, J.A., Batson, B., Butts, J.A., Chao, J.C., Deneroff, M.M., Dror, R.O., Even, A., Fenton, C.H. and Forte, A, Anton 2: Raising the Bar for Performance and Programmability in a Special-Purpose Molecular Dynamics Supercomputer. *IEEE Press* **2014**, 41-53.

77. Shan, Y. B.; Klepeis, J. L.; Eastwood, M. P.; Dror, R. O.; Shaw, D. E., Gaussian split Ewald: A fast Ewald mesh method for molecular simulation. *J Chem Phys* **2005,** *122* (5).

78. Krivov, G. G.; Shapovalov, M. V.; Dunbrack, R. L., Jr., Improved prediction of protein side-chain conformations with SCWRL4. *Proteins* **2009,** *77* (4), 778-95.

79. Sethi, A.; Eargle, J.; Black, A. A.; Luthey-Schulten, Z., Dynamical networks in tRNA:protein complexes. *Proceedings of the National Academy of Sciences* **2009,** *106* (16), 6620-6625.

80. Girvan, M.; Newman, M. E. J., Community structure in social and biological networks. *Proceedings of the National Academy of Sciences* **2002,** *99* (12), 7821-7826.

81. Rostovtseva, T. K.; Gurnev, P. A.; Protchenko, O.; Hoogerheide, D. P.; Yap, T. L.; Philpott, C. C.; Lee, J. C.; Bezrukov, S. M., alpha-Synuclein Shows High Affinity Interaction with Voltage-dependent Anion Channel, Suggesting Mechanisms of Mitochondrial Regulation and Toxicity in Parkinson Disease. *J Biol Chem* **2015,** *290* (30), 18467-77.

82. Alcaraz, A.; Nestorovich, E. M.; Lopez, M. L.; Garcia-Gimenez, E.; Bezrukov, S. M.; Aguilella, V. M., Diffusion, Exclusion, and Specific Binding in a Large Channel: A Study of OmpF Selectivity Inversion. *Biophys J* **2009,** *96* (1), 56-66.

83. Hille, B., *Ion channels of excitable membranes*. 3rd ed.; Sinauer: Sunderland, Mass., 2001; p xviii, 814 p.

84. Kabsch, W., XDS. *Acta Crystallographica Section D Biological Crystallography* **2010,** *66* (2), 125-132.

85. Kabsch, W., Integration, scaling, space-group assignment and post-refinement. *Acta Crystallographica Section D Biological Crystallography* **2010,** *66* (2), 133-144.

86. Evans, P. R., An introduction to data reduction: space-group determination, scaling and intensity statistics. *Acta Crystallographica Section D Biological Crystallography* **2011,** *67* (4), 282-292.

87. Evans, P. R.; Murshudov, G. N., How good are my data and what is the resolution? *Acta Crystallographica Section D Biological Crystallography* **2013,** *69* (7), 1204-1214.

88. Mccoy, A. J.; Grosse-Kunstleve, R. W.; Adams, P. D.; Winn, M. D.; Storoni, L. C.; Read, R. J., Phaser crystallographic software. *J Appl Crystallogr* **2007,** *40* (4), 658-674.

89. Emsley, P.; Cowtan, K., Coot: model-building tools for molecular graphics. *Acta Crystallographica Section D Biological Crystallography* **2004,** *60* (12), 2126-2132.

90. Kovalevskiy, O.; Nicholls, R. A.; Long, F.; Carlon, A.; Murshudov, G. N., Overview of refinement procedures within REFMAC5: utilizing data from different sources. *Acta Crystallographica Section D Structural Biology* **2018,** *74* (3), 215-227.

91. Murshudov, G. N.; Skubák, P.; Lebedev, A. A.; Pannu, N. S.; Steiner, R. A.; Nicholls, R. A.; Winn, M. D.; Long, F.; Vagin, A. A., REFMAC5 for the refinement of macromolecular crystal structures. *Acta Crystallographica Section D Biological Crystallography* **2011,** *67* (4), 355-367.

92. Pettersen, E. F.; Goddard, T. D.; Huang, C. C.; Couch, G. S.; Greenblatt, D. M.; Meng, E. C.; Ferrin, T. E., UCSF Chimera-A visualization system for exploratory research and analysis. *Journal of Computational Chemistry* **2004,** *25* (13), 1605-1612.

Table of Contents Graphic